PHYSICAL REVIEW B **102**, 035135 (2020)

Spectral function of an electron coupled to hard-core bosons

J. Bonča
Faculty of Mathematics and Physics, University of Ljubljana, 1000 Ljubljana, Slovenia
and J. Stefan Institute, 1000 Ljubljana, Slovenia

(Received 18 February 2020; revised 8 July 2020; accepted 8 July 2020; published 20 July 2020)

We have computed static and dynamic properties of an electron coupled to hard-core-boson (HCB) degrees of freedom in one spatial dimension. The polaron, an electron dressed with HCB excitations, remains light even in the strong-coupling limit as its effective mass remains of the order of the free-electron mass. This result is in a sharp contrast to the Holstein model where the electron effective mass increases exponentially with the electron-phonon coupling. HCB degrees of freedom mediate the attractive potential between two electrons that form a bound singlet bipolaron state at any nonzero coupling strength. In the low-frequency regime of the electron spectral function we observe a quasiparticle (QP) band that is separated from the continuum of states only in the central part of the Brillouin zone. The quasiparticle weight approaches zero as the QP band enters the continuum where it obtains a finite lifetime. At finite temperature an electron can annihilate thermally excited HCBs. Such thermally activated processes lead to a buildup of the spectral weight below the QP band. While the investigated model bears a resemblance with the Holstein model, we point out many important differences that originate from the binary HCB excitation spectrum, which in turn mimics spin-$\frac{1}{2}$ degrees of freedom.

DOI: 10.1103/PhysRevB.102.035135

I. INTRODUCTION

We investigate the static, dynamic, and thermodynamic properties of an electron coupled to hard-core-boson (HCB) degrees of freedom. The model under the investigation resembles the well-known Holstein model (HM) [1], which has been a subject of extensive research [2–20]. Starting from the HM, the HCB model (HCBM) is obtained by replacing each oscillator with its infinite degrees of freedom by a HCB representing a state that can be either occupied or unoccupied. Despite a significant reduction of inelastic degrees of freedom in comparison to the HM, the statistics of neighboring energy-level spacings in HCBM remains well described by the Wigner-Dyson distribution [21], characteristic of nonintegrable ergodic quantum models. The reduction of HM to HCBM has further important consequences: HCBM possess a limited energy spectrum which further facilitates finite-temperature studies, reduction of inelastic degrees of freedom allows studies of larger-size systems approaching closer the thermodynamic limit.

An important motivation for the research presented in this paper originates from the research into high-temperature superconductivity where the quest for the origin of the attractive interaction between charge carriers is still active. Among the fundamental open questions is whether the attractive interaction is based on lattice degrees of freedom or is due to the strong Coulomb interaction that generates the spin-exchange coupling. Since the binary spectrum of HCBs closely resembles a spin-$\frac{1}{2}$ degree of freedom, HCBM can be used to simulate properties of a spin-polaron [22–24], i.e., electron, interacting with spin degrees of freedom and thus bridging the gap between research into lattice and spin models.

So far, physical realization of systems with HCBs is limited to ultracold atoms in optical lattices [25,26]. Nevertheless, models where electrons are coupled to HCBs may carry potential relevance to microscopic mechanisms of superconductivity. As we show in this paper, the effective polaron mass remains small even in the limit of very strong electron-HCB coupling strength. We also demonstrate that HCBs can mediate the necessary attractive potential for the formation of light bipolarons.

II. MODEL AND METHOD

We analyze a model with a single electron in a one-dimensional chain of size L with periodic boundary conditions coupled to HCB degrees of freedom,

$$H = -t_0 \sum_j (c_j^\dagger c_{j+1} + \text{H.c.}) - g \sum_j \hat{n}_j (b_j^\dagger + b_j) + \omega_0 \sum_j b_j^\dagger b_j, \tag{1}$$

where $c_j^\dagger$ and $b_j^\dagger$ are electron and HCB creation operators at site j, respectively, and $\hat{n}_j = c_j^\dagger c_j$ represents the electron-density operator. HCBs are defined via the following commutation relation $[b_i, b_j^\dagger] = \delta_{i,j}(1 - 2b_i^\dagger b_i)$. Parameter g measures the strength of coupling between the electron and HCB, ω_0 denotes a dispersionless optical HCB frequency, and t_0 nearest-neighbor hopping amplitude. From here on we set $t_0 = 1$.

In most calculations we have used a full translationally invariant Hilbert space spanning $N_{\text{st}} = 2^L$ basis states. In case of zero-T calculations we have implemented the standard Lanczos [27] technique. To determine static and dynamic properties of the model at finite-T we have implemented the finite temperature Lanczos method (FTLM) as described in Refs. [28,29] where it has been shown that static

©2020 American Physical Society

thermodynamic properties of an operator A can be evaluated via sampling over random states $|r\rangle$ defined in a subspace with one electron and multiple HCB degrees of freedom,

$$\langle A\rangle_T = \mathcal{Z}^{-1}\sum_{r=1}^{R}\sum_{j=1}^{M} e^{-\beta\epsilon_j}\langle r|\psi_j\rangle\langle\psi_j|A|r\rangle,$$

$$\mathcal{Z} = \sum_{r=1}^{R}\sum_{j=1}^{M} e^{-\beta\epsilon_j}|\langle r|\psi_j\rangle|^2, \tag{2}$$

where $|\psi_j\rangle$ and ϵ_j are Lanczos wave functions and corresponding energies, respectively, in the subspace with one electron, $\beta = 1/T$, and $\mathcal{Z}$ is the partition function. Furthermore, R represents the number of different random states, and M is the number of Lanczos iterations.

The main goal of this work is to analyze the single-electron spectral function, corresponding to electron addition, as obtained via the corresponding retarded Green's function

$$A(\omega, k) = -\pi^{-1}\lim_{\eta\to 0^+}\mathcal{G}^R(\omega + i\eta, k), \tag{3}$$

where, at finite T, $\mathcal{G}^R(\omega + i\eta, k)$ is obtained via the Gibbs ensemble,

$$\mathcal{G}^R(\omega, k) = \mathcal{Z}^{-1}\int_0^\infty dt e^{i\omega t}\sum_n e^{-\beta\epsilon_n^0}\langle\phi_n^0|c_k(t)c_k^\dagger(0)|\phi_n^0\rangle, \tag{4}$$

where ϕ_n^0 are multi-HCB eigenstates of the Hamiltonian in Eq. (1) with no electron present in the system, while ϵ_n^0 are the corresponding energies and $c_k = 1/\sqrt{L}\sum_{j=1}^{L}\exp(ikj)c_j$. We finally take advantage of the FTLM method [28] and replace the trace over a complete set of states $|\phi_n^0\rangle$ by the summation over random states $|r^0\rangle = \sum_{n=1}^{N_0}\alpha_n|\phi_n^0\rangle$, where α_n are distributed randomly, and

$$A(\omega, k) = \mathcal{Z}^{-1}\sum_{r=1}^{R}\sum_{n=1}^{N_0}\sum_{j=1}^{M} e^{-\beta\epsilon_n^0}\langle r^0|\phi_n^0\rangle\langle\phi_n^0|c_k|\psi_j\rangle$$
$$\times\langle\psi_j|c_k^\dagger|r^0\rangle\delta(\omega - \epsilon_j + \epsilon_n^0), \tag{5}$$

where $|\psi_j\rangle$ and ϵ_j are Lanczos wave functions and the corresponding energies, respectively, in the subspace with one electron. Lanczos states are generated starting from states $c_k^\dagger|r^0\rangle$. Furthermore, $R \approx 100$ represents the number of different random states, $N_0 = 2^L$ is the size of the Hilbert space in the zero-electron subspace, and M is the number of Lanczos iterations. We have used typically $M = 50$ Lanczos iterations to obtain static properties at finite T and $M = 500$ for dynamic quantities combined with the Gram-Schmidt orthogonalization procedure to avoid spurious nonorthogonal states that appear at large values of M. The Lorentzian form of the δ functions with the half-width at half maximum (HWHM) η was used for graphic representations of $A(k, \omega)$.

While our calculations were limited to rather small system sizes $L = 16$, we have expanded our calculations from using only periodic boundary conditions towards the twisted boundary conditions [20,30–32] that are equivalent to the introduction of the magnetic flux penetrating the ring. In this approach, the kinetic-energy term in Eq. (1) is transformed to $H_{\rm kin} = -t_0\sum_j(c_j^\dagger c_{j+1}e^{i\theta} + \text{H.c.})$, where θ represents a magnetic flux that penetrates the ring $\phi_m = \theta L/2\pi$ in units of h/e_0. Discrete k points $k_n = 2\pi n/L$ can thus be connected by choosing $\theta \in [0, 2\pi/L]$.

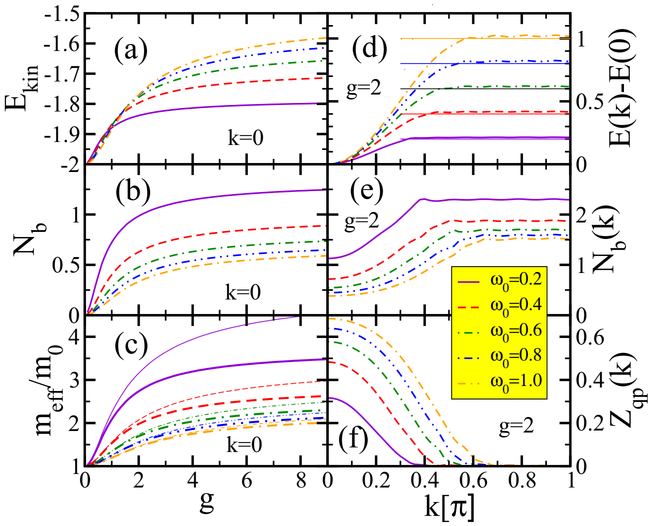

FIG. 1. Ground-state properties computed by using full basis on a ring with $L = 16$ taking into account the full translational symmetry: (a) the kinetic energy $E_{\rm kin} = \langle\psi_k| - t_0\sum_j c_j^\dagger c_{j+1} + \text{H.c.}|\psi_k\rangle$ vs g at different ω_0, (b) the total number of HCBs $N_b = \langle\psi_k|\sum_j b_j^\dagger b_j|\psi_k\rangle$, and (c) the effective mass $m_{\rm eff} = (\partial^2E(k)/\partial k^2|_{k=0})^{-1}$ compared with the free-electron mass $m^0 = 1/2t_0$ where $E(k) = \langle\psi_k|H|\psi_k\rangle$, where $|\psi_k\rangle$ is the ground-state polaron wave function with momentum k. Thin lines represent the inverse of the quasiparticle weight defined as $Z_{\rm qp}(k) = |\langle\psi_k|c_k^\dagger|\emptyset\rangle|^2$ at $k = 0$ where $|\emptyset\rangle$ is the state with no electron and no HCB excitations. In panels (d) through (f) we show k-dependent properties at fixed coupling g of the total energy $E(k)$ in panel (d), $N_b(k)$ in panel (e), and the quasiparticle weight $Z_{\rm qp}(k)$ in panel (f). Horizontal lines in panel (d) indicate values of ω_0.

Further details concerning the construction of the translationally invariant basis states and comparison of the selected ground-state properties between a small basis set and a full basis can be obtained in Appendix A. We show in the Appendix B that finite-size effects seem to be well under control in all temperature regimes by comparing $A(k, \omega)$ computed on two different system sizes and different T. In the Sec. III E we also compute the lowest-frequency moments of $A(k, \omega)$ and compare them with analytical results that are free of finite-size effects, which in turn renders further insight into the applicability of FTLM to the model under the investigation.

III. RESULTS

A. Zero-*T* properties

In Figs. 1(a) through 1(c) we show some characteristic ground-state properties of the model at $k = 0$. With increasing electron-boson coupling g the kinetic energy $E_{\rm kin}$ increases but shows a tendency toward saturation at larger g, as seen in Fig. 1(a). $E_{\rm kin}$ also increases with increasing ω_0 at fixed g which stands in contrast to a decrease of the total number N_b of HCBs with increasing ω_0, seen in Fig. 1(b). Further elaborating on results at fixed g: at smaller ω_0 the electron is dressed up with a larger number of HCB excitations than at larger values of ω_0; nevertheless, its kinetic energy is less affected by the presence by the HCB cloud at smaller ω_0. It is furthermore instructive to compare the slow increase of N_b with increasing g to the increase of the number of phonons in the strong-coupling limit in the HM where $N_{\rm ph} = (g/\omega_0)^2$. This profound difference between the two models is trivially explained since the maximal on-site occupancy of HCBs is limited to 1. In Fig. 1(c) we display the effective polaron mass $m_{\rm eff}$. In the small-g limit, perturbation theory can be applied and results in the following polaron dispersion relation:

$$E(k) = \epsilon(k) + \frac{1}{L}\sum_q \frac{g^2}{\epsilon(k) - \epsilon(k+q) - \omega_0}, \qquad (6)$$

where $\epsilon(k) = -t_0\cos(k)$ is the free-electron dispersion relation. In this limit, $m_{\rm eff}/m_0 - 1 \propto g^2$ just as in the HM, while at larger g it displays a slow sublogarithmic increase with g. Here, the difference with the HM is even more pronounced since it is well known that, in the strong-coupling limit of the HM, $m_{\rm eff}/m_0 = \exp[(g/\omega_0)^2]$. In the case of the HM, $m_{\rm eff}$ can be determined from $Z_{\rm qp}(k=0)^{-1} = m_{\rm eff}/m_0$, as shown in Ref. [9]. In Fig. 1(c) we show along $m_{\rm eff}/m_0$ also $Z_{\rm qp}^{-1}$. The agreement between both quantities is good for large ω_0 at any g, but starts to deviate strongly at small ω_0.

In Figs. 1(d) through 1(f) we show k-dependent properties of the electron coupled to HCBs at fixed $g = 2$ and various ω_0. We start with the discussion of the dispersion relation representing the polaron energy $E(k) = \langle\psi_k|H|\psi_k\rangle$, where $|\psi_k\rangle$ is the ground-state polaron wave function with momentum k, shifted by $E(k=0)$ which facilitates a quantitative comparison between results corresponding to different values of ω_0, as shown in Fig. 1(d). Common to all cases is a quadratic increase at small k followed by an abrupt flattening of the band at a value of k_0 corresponding to $E(k_0) - E(0) = \omega_0$. It seems as if the polaron band, also known as the quasiparticle (QP) band intercepts the continuum of states that starts at the energy ω_0 above $E(0)$. This is in a sharp contrast to the Holstein-polaron case where the QP band remains separated from the continuum in the whole Brillouin zone. A similar k dependence is observed in the mean HCB number $N_b(k)$, Fig. 1(e). The QP weight $Z_{\rm qp}(k)$ provides information about the electronic character of the polaronic state. In Fig. 1(f) we observe the disappearance of $Z_{\rm qp}$ at k_0 where the QP band enters the continuum. This result suggests that the ground state $|\psi_k\rangle$ for $k > k_0$ contains nearly zero free-electron contribution of a state $c_k^\dagger|\emptyset\rangle$. Instead, $|\psi_k\rangle$ is composed of a polaron in the state $k = 0$ that contains a significant amount of the free-electron wave function $c_{k=0}^\dagger|\emptyset\rangle$, and an extra HCB excitation in the state k. This is further consistent with results presented in Fig. 2 where we show the electron kinetic energy $E_{\rm kin}(k) = \langle\psi_k|H_{\rm kin}|\psi_k\rangle$. Naively, one would expect $E_{\rm kin}(k)$ to resemble a renormalized free-electron dispersion relation. In contrast, $E_{\rm kin}(k)$ shows a nonmonotonic behavior whereby, at larger $k > k_0$, it again reaches its value at zero momentum, i.e., $E_{\rm kin}(k=0) \sim E_{\rm kin}(k > k_0)$, consistent with the above hypothesis.

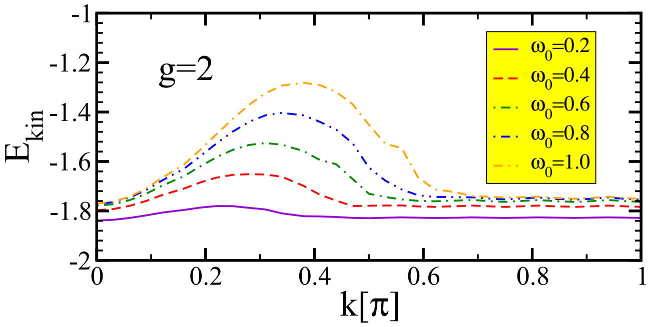

FIG. 2. Electron kinetic energy $E_{\rm kin}$ vs k at different ω_0.

Before switching to the description of finite-T properties of the HCBM we show that the electron-HCB interaction leads to a formation of bound pairs of polarons or bipolarons. To test this assumption we investigate a system with two electrons coupled with HCBs in the presence of a Coulomb on-site interaction U

$$H = -t_0 \sum_{j,\sigma\in[\uparrow,\downarrow]} (c_{j,\sigma}^\dagger c_{j+1,\sigma} + \text{H.c.}) - g\sum_j \hat{n}_j(b_j^\dagger + b_j) + U\sum_j n_{j\uparrow}n_{j\downarrow} + \omega_0\sum_j b_j^\dagger b_j, \qquad (7)$$

where $n_j = n_{j\uparrow} + n_{j\downarrow}$ and $n_{j,\sigma} = c_{j,\sigma}^\dagger c_{j,\sigma}$. We have computed the binding energy of a bipolaron defined as $\Delta = E_2 - 2E_1$ where E_2 is the ground-state energy of two electrons with opposite spin orientation and E_1 is the ground-state energy of a system with one electron. In Fig. 3 we present Δ vs g for different values of the HCB frequency ω_0. The results show that at $U = 0$ the bipolaron remains bound irrespective of the coupling strength as well as ω_0 while at finite $U = 1$ there exists a critical value of g_c. This result is consistent with Δ computed in the atomic limit, i.e., at $t_0 = 0$ where we obtain

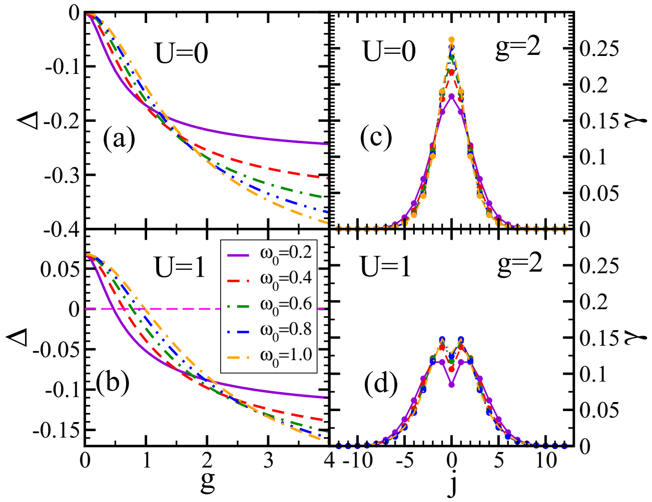

FIG. 3. Δ vs g for different values of ω_0 as shown in the legends for $U = 0$ and 1 in panels (a) and (b), respectively. In panels (c) and (d), we present $\gamma(j)$ at fixed $g = 2$ while the other parameters of the model are the same as in panels (a) and (b). All results were computed on a system with 13 sites using periodic boundary conditions.

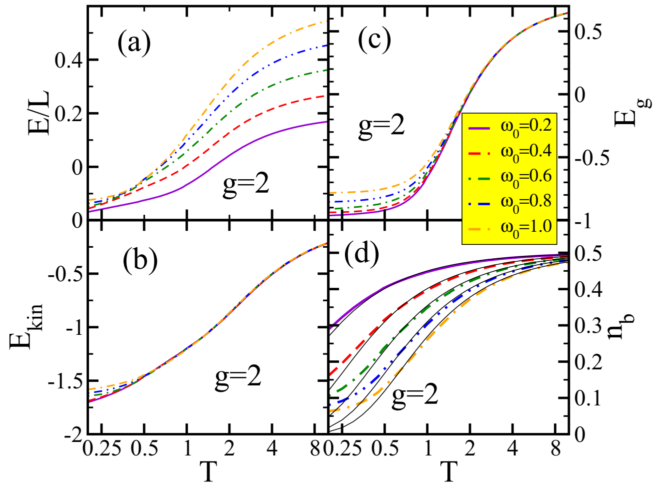

FIG. 4. Finite-T properties of selected expectation values computed on a system with $L = 16$ presented on a semilog plot. In panel (a) we present the energy of the system $E(T) = \langle H\rangle_T$ per site L where the expectation value is taken by using the FTLM method, as described in Eq. (2). Similarly, in panel (b), we present $E_{\rm kin}(T)$, in panel (c) we display the electron-HCB coupling part of the Hamiltonian in Eq. (1): $E_g = -\langle g\sum_j \hat{n}_j(b_j^\dagger + b_j)\rangle_T$, and in panel (d) the number of HCB per site $n_b = N_b/L$ along with the HCB thermal distribution functions $n_b^0 = \frac{1}{\exp[\beta\omega_0]+1}$, shown using thin black lines.

the following expression for the binding energy:

$$\Delta = \sqrt{4g^2 + \omega_0^2} - \tfrac{1}{2}\sqrt{16g^2 + \omega_0^2} - \omega_0/2 + U, \tag{8}$$

which leads to $\Delta < 0$ for $U = 0$ at arbitrary $|g| > 0$.

To get further insight into the shape of the bipolaron we also present in Fig. 3 the density-density correlation function

$$\gamma(j) = \frac{\sum_i \langle\psi_0|n_i n_{i+j}|\psi_0\rangle}{\sum_{i,l}\langle\psi_0|n_i n_{i+l}|\psi_0\rangle}, \tag{9}$$

defined so as $\sum_j \gamma(j) = 1$. The $\Delta < 0$ regime is reflected in an exponentially decaying form of $\gamma(j)$. At finite U the bound state is formed from two electrons positioned predominantly on neighboring sites. This results bears a similarity to a $S1$ bipolaron in the Holstein-Hubbard model [33–36].

B. Finite-*T* properties

In Fig. 4 we present selected thermodynamic properties of the model. The total energy of the system increases with T as well as with ω_0; see Fig. 4(a). This is in part due to the thermal increase of the average HCB site occupation number n_b. The other contribution comes from the increase of the kinetic energy $E_{\rm kin}$, shown in Fig. 4(b), that with increasing T approaches its high-T limit $E_{\rm kin} = 0$. Unexpectedly, $E_{\rm kin}$ shows very weak dependence on the HCB frequency ω_0 except at very small T. Likewise, the electron-HCB coupling part of the Hamiltonian, E_g as shown in Fig. 4(c) increases with T and even changes sign, also displays very little dependence on ω_0 above $T \gtrsim 1$. The HCB occupancy per site n_b closely follows the Fermi-Dirac-like distribution, characteristic for HCBs $n_b^0 \sim 1/[\exp(\beta\omega_0) + 1]$, as shown in Fig. 4(d) by thin black lines. In the high-T limit, i.e., for $T \gg \omega_0$, numerical results clearly approach $n_b \to 1/2$.

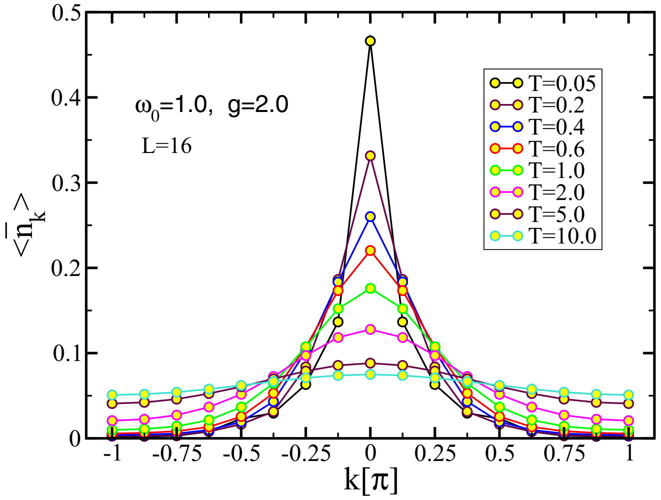

FIG. 5. The single-particle density matrix $\bar{n}_k$ vs T computed by using $\omega_0 = 1$, $g = 2$, and $L = 16$.

In Fig. 5 we present the single-particle density matrix $\bar{n}_k$ defined as $\langle c_k^\dagger c_k\rangle_T$ where the thermal average is taken in the subspace with one electron. In addition, $\bar{n}_k$ represents the sum rule of the electron-removal spectral function. In the case of the free electron, i.e., at $g = 0$, $\bar{n}_k(T = 0) = \delta_{k,0}$, while at finite $g > 0$, $\bar{n}_k(T = 0)$ remains centered around $k = 0$ but obtains a finite width in momentum space. With increasing T its width increases and in the $T \to \infty$ limit approaches a constant $\bar{n}_k = 1/L$. We should also stress that, besides the sum rule $\sum_k \bar{n}_k = 1$ there exists another slightly less obvious relation $-2t_0\sum_k \cos(k)\bar{n}_k = E_{\rm kin}(T)$.

C. Spectral functions *A*(*k*, *ω*)

In Fig. 6 we present density plots representing $A(\omega, k)$ in the entire Brillouin zone (BZ) at fixed coupling $g = 2$ and two different sets of $\omega_0 = 1$ and 0.2. For a more quantitative analysis we also display with dashed lines the corresponding ground-state polaron energy $E(k) = \langle\psi_k|H|\psi_k\rangle$, where $|\psi_k\rangle$ is the ground-state polaron wave function with momentum k. We focus first on $\omega_0 = 1$ and small $T/\omega_0 = 0.05$ where we clearly observe in the low-ω regime the QP band only in a limited part of the Brillouin zone, $k \in [-0.6\pi, 0.6\pi]$. The spectral weight of the QP band is given by $Z_{\rm qp}(k)$. Outside this interval the QP band enters the continuum of states and $Z_{\rm qp}$ approaches zero, also consistent with Figs. 1(d) and 1(f).

In the Appendix B we show that only a partial separation of the QP band from the continuum is a consequence of the HCB commutation relation. In a model where the Hilbert space of the HCBM is expanded to contain up to two phonon degrees of freedom per site, the QP band remains visible throughout the entire BZ and approaches the lower edge of the continuum near the edge of the BZ.

This behavior is in a sharp contrast to the HM case where the QP band extends through the whole BZ and is entirely located below the continuum [9,16–20]. Within the incoherent part of the spectra we observe a rather-well-defined band of

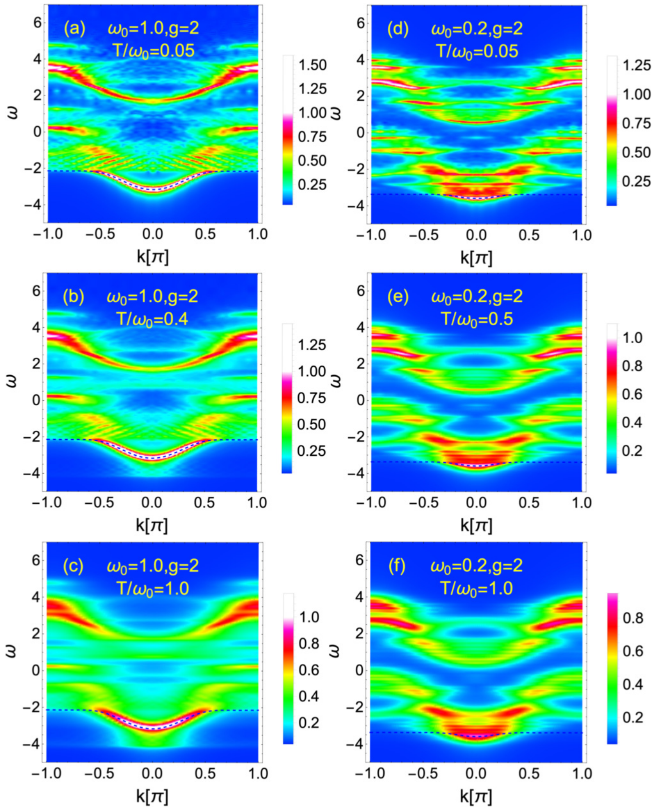

FIG. 6. $A(\omega, k)$ for $g = 2$ vs different values of T/ω_0 presenting two sets of results in parallel for $\omega_0 = 1$ in panels (a) through (c) and $\omega_0 = 0.2$ in panels (d) through (f). The same size of the system $L = 16$ was used as in Fig. 1. In addition we have used twisted boundary conditions to compute $A(\omega, k)$ at 25 equally spaced k points in the interval $k \in [0, \pi]$ with increments of $\Delta k = \pi/24$. Moreover, in all figures from panels (a) to (f), the same color coding is used to enable direct comparison between different cases. In all figures we also display the polaron dispersion relation at zero-T $E(k)$ using a dashed line as a guide to the eye. Lorentzian broadening $\eta = 0.05$ was used in all cases.

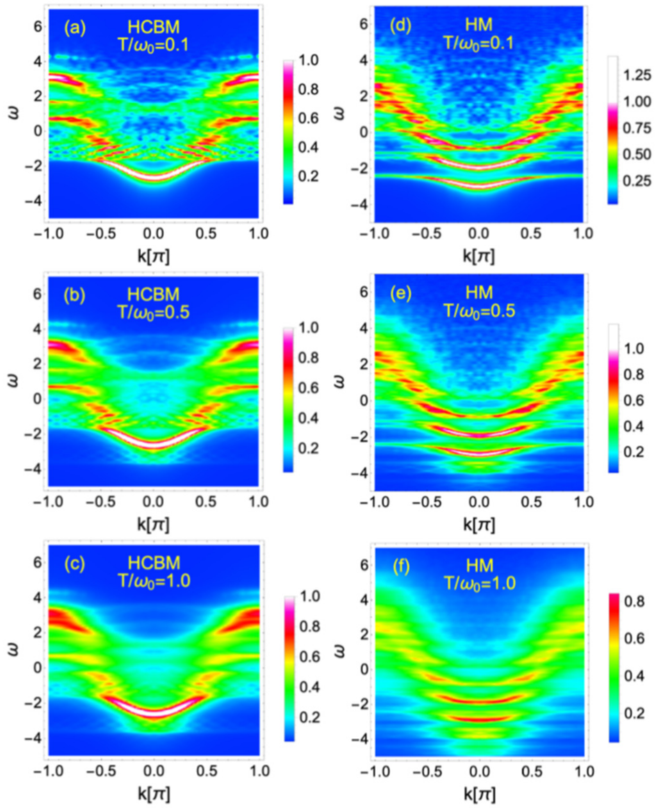

FIG. 7. Comparison of $A(\omega, k)$ for $\omega_0 = 1$ and $g = \sqrt{2}$ or $\lambda = g^2/(2\omega_0 t_0) = 1$ vs different values of T/ω_0 for two different models. The dimensionless coupling constant λ in the HM case at $\lambda = 1$ represents the intermediate coupling regime. From panels (a) through (c), for the HCBM and from panels (d) through (f) for the HM. The latter set of results was computed by using a Hamiltonian as defined in Eq. (1) but with standard boson commutation relations $[b_i, b_j^\dagger] = \delta_{i,j}$ and by using the method described in Ref. [20]. In all panels from (a) to (f) we have used identical color coding to enable direct comparison between different cases. Lorentzian broadening $\eta = 0.05$ was used in all cases.

high-energy excitations with its maximal intensity around the edges of the BZ. The separation between between the QP band and these high-energy excitations can be estimated from the energies computed in the atomic limit of the model, i.e., at $t_0 = 0$:

$$\epsilon^{\pm}_{t_0=0} = \tfrac{1}{2}\left(\omega_0 \pm \sqrt{\omega_0^2 + 4g^2}\right), \tag{10}$$

which gives the energy gap $\Delta_{\text{gap}} = (\omega_0^2 + 4g^2)^{1/2} = 4.1$, which further determines an estimate of the separation between the two bands. With increasing T additional spectral weight develops below the QP band predominantly around the center of the BZ, as seen in Figs. 6(b) and 6(c). This buildup of the spectra below the QP band appears because at elevated T an electron can annihilate a thermally excited HCB.

Remnants of the QP band remain clearly distinguishable even at $T = \omega_0$, the same holds also for the well-pronounced peaks around the edges of the BZ in the high-frequency regime. In contrast to the HM case, the extra spectral weight that develops below the QP band extends only ω_0 below the bottom of the QP band, consistent with the fact that only a single HCB is allowed per site.

In spectral functions at small $\omega_0 = 0.2$, shown in Figs. 6(d) through 6(f), the QP band is barely visible even at small $T/\omega_0 = 0.05$, it merges with the continuum around $k \approx 0.35\pi$. This is also consistent with the behavior of Z_{qp}, shown in Fig. 1(f), which at $k \approx 0.35\pi$ approaches zero. In contrast with the $\omega_0 = 1$ case where the QP band is well separated from the incoherent continuum, at $\omega_0 = 0.2$ we find rather large spectral weight just above the QP band. Towards the edge of the BZ the incoherent part of the spectrum consists of a series of separated and split bands.

In Fig. 7 we compare between $A(\omega, k)$ as obtained from the HCBM and the standard HM using identical model parameters. The most notable distinction is observed already at small $T/\omega_0 = 0.1$, as shown in Figs. 7(a) and 7(d). While in the HCBM, a single well-defined QP band in the vicinity of the center of the BZ is observed, in the HM there are multiple well-defined bands separated by ω_0 above the QP band extending throughout the entire BZ. Spacing between

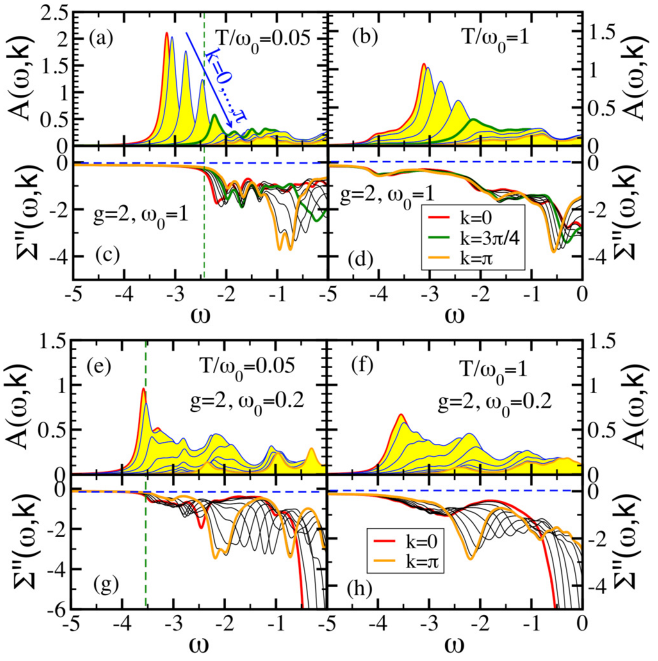

FIG. 8. $A(\omega, k)$ and $\Sigma(\omega, k)$ for $g = 2$ and $\omega_0 = 1$ and 0.2 computed at two distinct values of $T/\omega_0 = 0.1$ in panels (a), (c), (e), (g) and 1.0 in panels (b), (d), (f), (h). The same size of system was used as in Figs. 1 through 6. In each figure we present nine curves computed at $k = m\pi/8$, $m = 0, \dots, 8$. Lorentzian broadening $\eta = 0.05$ was used in all cases, which is also responsible for a small deviation from zero in Fig. 8(c) for $\omega \lesssim -2.5$.

multiple bands observed in the case of HM model can be explained by inspecting the energy spectra in the atomic limit of the model given by $\epsilon^n_{t_0=0} = -g^2/\omega_0 + n\omega_0$. In addition, we find larger effective mass in the HM that is reflected in a less dispersive QP band in comparison with the HCB case. A quantitative analysis yields a mass ratio $m^{\mathrm{HM}}_{\mathrm{eff}}/m^{\mathrm{HCB}}_{\mathrm{eff}} \approx 1.6$.

Shifting now the comparison to finite-T results we observe additional spectral weight that emerges with increasing T below the respective QP bands in both cases. Nevertheless, in the HCBM the latter is limited to the energy interval $[E(k), E(k) - \omega_0]$ and remains restricted to the center of the BZ while in the HM case it appears as replicas of the nearly flat QP bands located at energies $E(k) - n\omega_0$ and with decreasing intensity as $n \in \mathcal{N}$ increases.

D. Self-energies

To study the lifetime of the QP peaks at elevated T, we have computed the corresponding self-energies. In Fig. 8 we show a direct comparison between a family of $A(\omega, k)$ obtained in the interval $k \in [0, \pi]$ and the imaginary parts of matching self-energies $\Sigma''(\omega, k)$ for two different values of $\omega_0 = 1$ and 0.2 at low $T/\omega_0 = 0.05$ as well as for high $T/\omega_0 = 1$. Results of $\Sigma''(\omega, k)$ were obtained from the relation $\mathcal{G}^R(\omega, k) = 1/[\omega - \epsilon(k) - \Sigma(\omega, k)]$, where $\epsilon(k)$ is the free-electron energy $\epsilon(k) = -2t_0 \cos(k)$. From comparison of Figs. 8(a) and 8(c) we notice that $\Sigma''(\omega, k) \approx 0$ in the frequency regime that corresponds to the well-defined QP band in Fig. 1(a). In Fig. 8(a) this regime, however, does not extend though the entire BZ since $\Sigma''(\omega, k)$ becomes finite already around $k_0 = 3\pi/4$ and at the value of ω corresponding to the lowest peak in $A(\omega, k_0)$. This behavior shows that a well-defined quasiparticle with an infinitely long lifetime exists only in a limited region of the BZ. In Fig. 8(g), corresponding to $\omega_0 = 0.2$ the regime of $\Sigma''(\omega, k) \approx 0$ is even more limited to the vicinity of the QP peak at $k = 0$. In both cases $\Sigma''(\omega, k)$ displays a rather pronounced k dependence which is in contrast to the HM case [20]. At elevated T, $\Sigma''(\omega, k)$ deviates significantly from zero already at frequencies corresponding to the positions of QP peaks, as seen in Figs. 8(d) and 8(h). This result demonstrates the importance of incoherent processes that originate from thermal collisions.

E. Frequency moments

We have computed the lowest frequency moments of the spectral function. As already shown in Refs. [19,20,37], frequency moments of the single polaron spectral function can be obtained analytically by using the following relation:

$$M_m(k) = \int_{-\infty}^{\infty} \omega^m A(\omega, k) \mathrm{d}\omega = \langle [[[c_k, H], H], \dots, H] c_k^\dagger \rangle_T, \tag{11}$$

where $\langle \dots \rangle_T$ represents the thermal average over zero-electron states and the number of commutators corresponds to the order of the frequency moment. Taking into account the HCB commutation relation $[b_i, b_j^\dagger] = \delta_{i,j}(1 - 2b_i^\dagger b_i)$, analytical expressions may be obtained for arbitrary moments even at finite T. Here we list just a few:

$$\begin{aligned} M_0(k) &= 1, \\ M_1(k) &= \epsilon(k), \\ M_2(k) &= \epsilon^2(k) + g^2, \\ M_3(k) &= \epsilon^3(k) + 2g^2\epsilon(k) + g^2\omega_0\left(1 - 2n_b^0\right), \end{aligned} \tag{12}$$

where $\epsilon(k) = -2t_0 \cos(k)$ and $n_b^0 = 1/[\exp(\omega_0/T) + 1]$. Note that $M_0(k)$ through $M_2(k)$ do not depend on T.

In Figs. 9 we plot $M_n(k)$; $n \in [1, 2, 3]$ extracted from $A(\omega, k)$ for a set of temperatures $T \in [0.2, 0.4, \dots, 2.0]$. Except for the smallest $T = 0.2$ and 0.4, numerically obtained frequency moments match nearly perfectly analytical predictions from Eq. (12) that are free of finite-size effects. A slight disagreement at low T could be the consequence of the discrete as well as limited frequency interval used in our calculations. It is instructive to note that the agreement with analytical predictions becomes even better at higher T, which further validates the applicability of the finite-T Lanczos procedure as well as the introduction of twisted boundary conditions. Attention should also be drawn to the notion that, in contrast with numerically obtained $M_n(k)$ from calculations on a finite-size system with $L = 16$, analytical results in Eq. (12) are free of finite-size effects. By applying twisted boundary conditions we were able to present $M_n(k)$ on 25 k points spaced by $\Delta k = \pi/24$ instead of on $L/2 + 1 = 9$ points when using periodic boundary conditions. We observe no spurious effects that might be expected due to twisted boundary conditions.

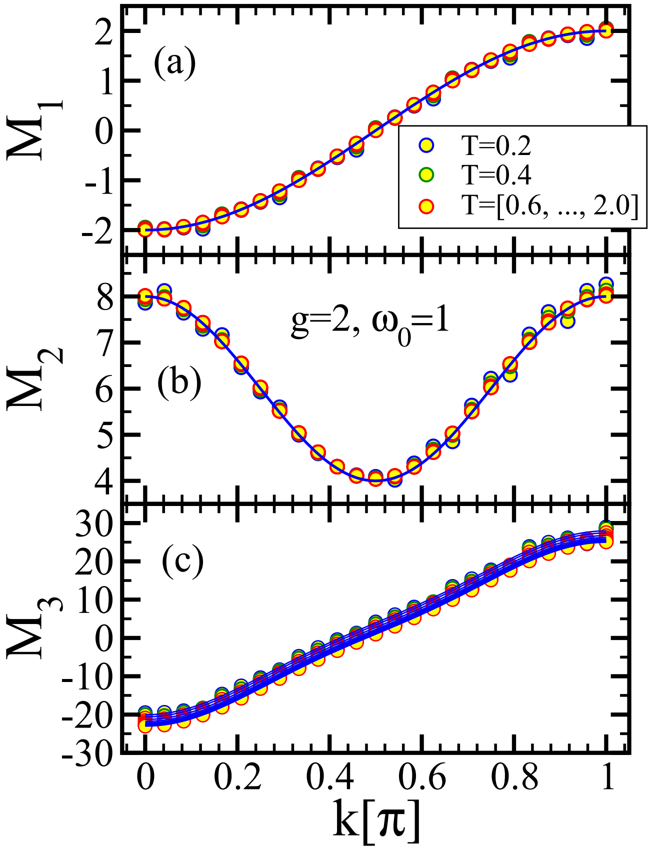

FIG. 9. $M_1(k), M_2(k)$, and $M_3(k)$ at $\omega_0 = 1$ and $g = 2$. In all plots we present with open symbols frequency moments obtained from numerical results of $A(\omega, k)$ computed on $L = 16$ sites system with twisted boundary conditions, just as in Fig. 6, but for ten different values of $T \in [0.2, 0.4, \ldots, 2.0]$. Results for the lowest $T = 0.2$ and 0.4 are represented with blue and green circles, respectively, while the rest of the results for $T \geqslant 0.6$ are shown in red. Blue lines represent analytic results from Eq. (12). In panel (c) we observe a slight downward shift of numerical data with increasing T, which is nearly perfectly captured by a set of thin lines representing $M_3(k)$ [Eq. (12)].

IV. SUMMARY

We have computed typical ground state as well as finite-T static and dynamic properties of an electron coupled to inelastic HCB degrees of freedom. While the model resembles a widely investigated HM, the limitation of infinite phonon degrees of freedom to HCBs brings about important differences. A polaron dressed with HCB excitations remains light, its effective mass remains of the order of the free-electron mass even in the limit of strong coupling. Still, the model remains within a class of nonintegrable models that exhibit ergodic properties at elevated temperatures.

In the electron spectral function we observe a dispersive QP peak forming a QP band with its maximal spectral weight centered around the center of the BZ. The peak remains separated from the continuum of states only in the central part of the BZ. With increasing momentum the weight of the QP band approaches zero as the peak enters the continuum while the imaginary part of the self-energy starts deviating from zero, which in turn signals the appearance of a finite lifetime. This result is in contrast with the HM where the QP band remains separated from the continuum throughout the whole BZ. With increasing T, additional features in the spectral function emerge in the form of additional spectral weight below the QP band already at temperatures below ω_0. These features appear due to processes where an electron annihilates one or more thermally excited HCBs.

As mentioned in the introduction, models where electrons are coupled to HCBs may carry potential relevance to microscopic mechanisms of superconductivity where the attraction between electrons is mediated by HCB degrees of freedom. Such mechanisms have been comprehensively investigated in connection with bipolaron formation mediated by lattice vibrations [7,35,36,38–40]. One of the shortcomings of these theories are exponentially large effective polaron and bipolaron masses in the strong electron phonon coupling regime. We have also shown that, in a system of two electrons with total spin $S = 0$ and in the absence of the on-site Coulomb interactions, a bound bipolaron exists at any finite HCB-electron coupling strength g. In the case of finite Coulomb interactions there exists a threshold value of g_c. Since the effective polaron mass remains small even in the limit of very strong electron-HCB coupling regime, HCB-mediated electron-electron interaction leads to the formation of light bipolarons.

ACKNOWLEDGMENTS

I acknowledge the support by the program P1-0044 of the Slovenian Research Agency, support from the Centre for Integrated Nanotechnologies, a U.S. Department of Energy, Office of Basic Energy Sciences user facility, and funding from the Stewart Blusson Quantum Matter Institute.

APPENDIX A

To gain further physical intuition into the ground-state properties of the HCBM as well as into the numerical approach used in this work, we have diagonalized the model in a restricted translationally invariant basis that spans only 14 states, obtained by acting with the off-diagonal part of Hamiltonian in Eq. (1), i.e.,

$$H_{\mathrm{off}} = H_{t_0} + H_g = -t_0 \sum_j (c_j^\dagger c_{j+1} + \mathrm{H.c.}) - g \sum_j \hat{n}_j (b_j^\dagger + b_j), \tag{A1}$$

N_h times on a state with a single electron in a translationally invariant state k with zero HCB degrees of freedom to obtain a limited basis set,

$$\left\{ \left| \phi_{k,l}^{(N_h)} \right\rangle \right\} = H_{\mathrm{off}}^{N_h} c_k^\dagger |\emptyset\rangle. \tag{A2}$$

Translationally invariant basis states are represented by HCB position coordinates i_j as $|i_1, i_2, \ldots, i_{N_{\mathrm{HCB}}}\rangle_k$, where N_{HCB} denotes the number of HCBs of a particular parent state. Due to the translational invariance, the electron position is kept fixed and does not need to be indexed. For the case of $N_h = 4$ we obtain 14 states: $|\emptyset\rangle_k = c_k^\dagger|\emptyset\rangle$, $|0\rangle_k$, $|\pm 1\rangle_k$, $|0, \pm 1\rangle_k$, $|\pm 2\rangle_k$,

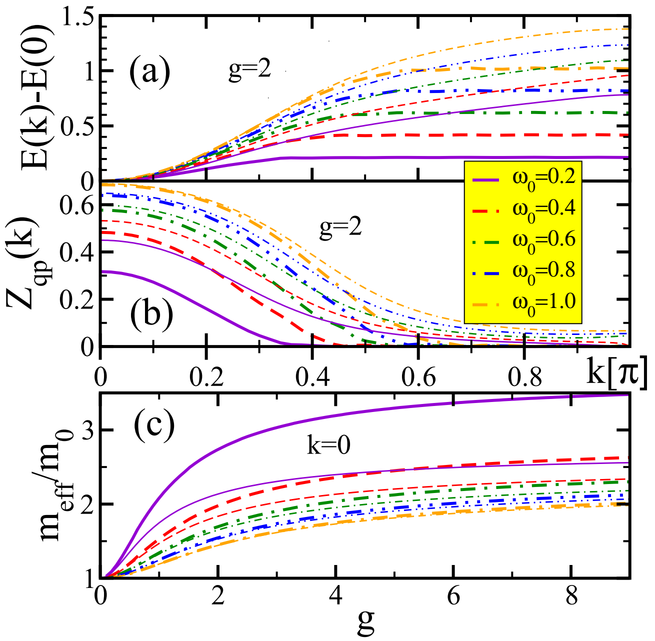

FIG. 10. Ground-state properties computed by using a full basis on a ring with $L = 16$ with $N_{\rm st} = 2^L$ parent states (thick lines) taking into account the full translational symmetry in comparison with calculations using only $N_{\rm st} = 14$ parent states (thin lines). Panels (a) and (b) show k-dependent energy $E(k) - E(0)$ and $Z_{\rm qp}(k)$, respectively, at fixed coupling g. Panel (c) shows the effective mass $m_{\rm eff}/m_0 = 2t_0(\partial^2E(k)/\partial k^2|_{k=0})^{-1}$ vs g.

$|\pm 3\rangle_k$, $|0, \pm 2\rangle_k$, $|1, 2\rangle_k$, $|-1, -2\rangle_k$. We next list just a few nonzero matrix elements:

$$\begin{aligned}
{}_k\langle \emptyset|H|\emptyset\rangle_k &= -2t_0\cos(k),\\
{}_k\langle 0|H|0\rangle_k &= {}_k\langle \pm 1|H|\pm 1\rangle_k = \omega_0, \dots,\\
{}_k\langle \emptyset|H|0\rangle_k &= {}_k\langle \pm 1|H|0 \pm 1\rangle_k = -g,\\
{}_k\langle 0|H|\pm 1\rangle_k &= {}_k\langle \pm 1|H|\pm 2\rangle_k = -t_0 e^{\mp ik},\\
{}_k\langle 0, \pm 1|H|0, \pm 1\rangle_k &= 2\omega_0.\\
&\cdots
\end{aligned} \tag{A3}$$

In Fig. 10 we show a comparison between results obtained by using a full translationally invariant basis (FB) on an $L = 16$ site system with $N_{\rm st} = 2^L$ states with those obtained by using only 14 limited basis states (LBSs) as listed above. Note also that results presented in the main body of the paper have been obtained by using the full translationally invariant basis. The only exemption from this rule is results of the HM presented in Fig. 7 where LBS states have been used combined with the standard Lanczos technique [27] and described in detail in Refs. [3,4]. Using LBS, we expectedly obtain consistently higher energies in comparison with the FB while it is also evident that differences between results decrease with increasing ω_0 at fixed coupling g. This consistently holds true for all quantities, shown in Fig. 10. It is rather surprising that the comparison of $m_{\rm eff}/m_0$ for the largest $\omega_0 = 1$ shows nearly identical results obtained by using substantially different numbers of basis states. Some of the main characteristics of ground-state properties may be discerned

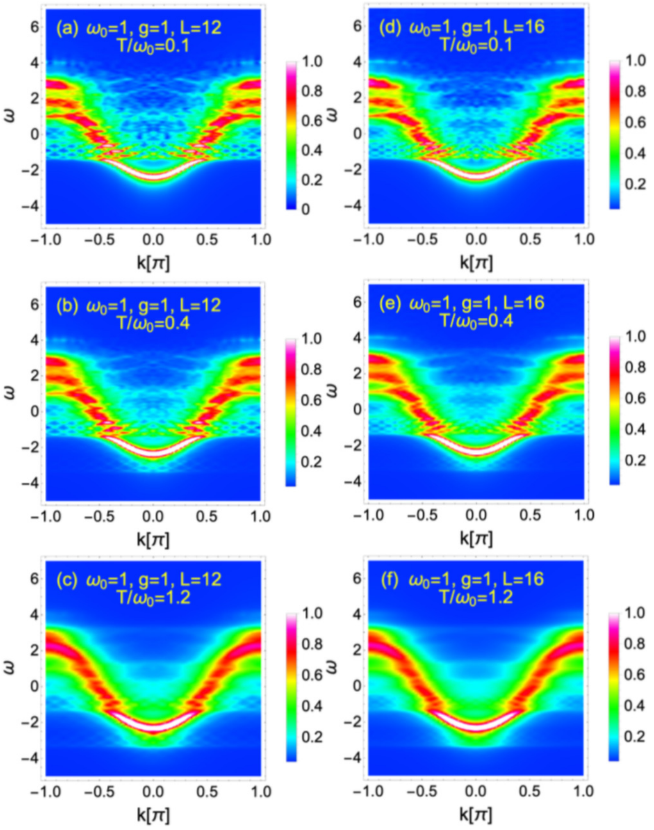

FIG. 11. $A(\omega, k)$ for $\omega_0 = 1$, $g = 2$ for two different system sizes $L = 12$ shown in panels (a) through (c) and $L = 16$ shown in panels (d) through (f) and three different values of T/ω_0 as specified in the panels. In all cases $A(\omega, k)$ was computed in 25 equally spaced nonequivalent k points in the interval $k \in [0, \pi]$ with increments of $\Delta k = \pi/24$. Note that, in all panels from (a) to (f) the same color coding was used to enable direct comparison between different cases.

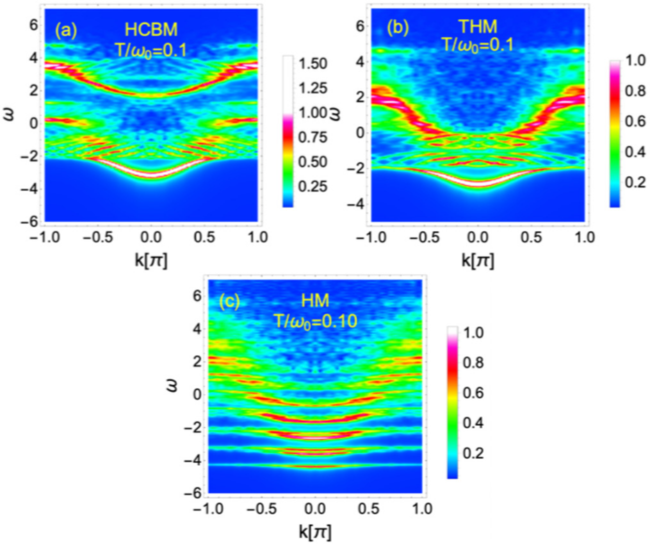

FIG. 12. $A(\omega, k)$ for $\omega_0 = 1$, $g = 2$ for (a) the HCBM, (b) the truncated HM (THM) with up to two phonon quanta per site, and (c) the HM with up to 22 phonon quanta per site.

even from considerably reduced LBS, such as a decrease of $Z_{\rm qp}(k)$ with increasing k and a slow increase of $m_{\rm eff}/m_0$ with g. Nevertheless, much larger systems with complete basis states are needed to obtain some of the most interesting properties of the polaron, such as the disappearance of the $Z_{\rm qp}(k)$ with increasing k, and crossing of the QP band with the continuum of states that is reflected in the flattening of $E(k)$ at k_0, given by the solution of $E(k_0) = E(0) + \omega_0$. In addition, using FB as opposed to LBS is necessary to investigate finite-T properties of the model where multiple HCB excitations are needed to properly describe thermally activated processes.

APPENDIX B: FINITE-SIZE ANALYSIS

We investigate the extent of finite-size effects on the spectral function. In Fig. 11 we present results obtained on two different systems with $L = 12$ and 16 sites. In both cases, $A(\omega, k)$ were computed on discrete k points according to periodic as well as twisted boundary conditions, equivalent to $k_{n,m} = 2\pi n/L + m\theta$ with $n \in [-L/2, L/2]$ and $\theta = 2\pi/(M_\theta L)$; $m \in [0, M_\theta - 1]$. For $L = 12$ and 16 systems we have chosen $M = 4$ and 3, respectively. As a result, for each system size $A(\omega, k)$ were computed by using $M_\theta * L/2 + 1$ nonequivalent k points. Despite substantially different system sizes, results are qualitatively identical at any T.

Finally, we follow the evolution of $A(\omega, k)$ with increasing number of allowed bosonic excitations per site starting from the HCBM in Fig. 12(a), over a truncated HM (THM) where we allow up to two phonon quanta per site, to the HM in Fig. 12(c) where we have expanded the Hilbert space up to a maximum of 22 phonon excitations per site. The emphasis of this analysis is on the evolution of the QP band. While in the HCBM the QP band enters the continuum at finite k_0, already in the HMR it flattens out and shows a tendency to disperse below the continuum almost towards the edge of the BZ, as seen in Fig. 12(b). Note that, in the case of the HM $g = 2$ represents the strong-coupling limit, $\lambda = 2$, where we observe a nearly flat QP band with a substantially reduced QP weight, followed by a series of nearly flat bands, separated by ω_0 as predicted by the strong-coupling theory.

[1] T. Holstein, Ann. Phys. (NY) **8**, 325 (1959).
[2] S. Engelsberg and J. R. Schrieffer, Phys. Rev. **131**, 993 (1963).
[3] J. Bonča, S. A. Trugman, and I. Batistić, Phys. Rev. B **60**, 1633 (1999).
[4] L. C. Ku, S. A. Trugman, and J. Bonča, Phys. Rev. B **65**, 174306 (2002).
[5] J. Ranninger and U. Thibblin, Phys. Rev. B **45**, 7730 (1992).
[6] F. Marsiglio, Phys. Lett. A **180**, 280 (1993).
[7] A. S. Alexandrov, V. V. Kabanov, and D. K. Ray, Phys. Rev. B **49**, 9915 (1994).
[8] H. Fehske, J. Loos, and G. Wellein, Z. Phys. B: Condens. Matter **104**, 619 (1997).
[9] H. Fehske, J. Loos, and G. Wellein, Phys. Rev. B **61**, 8016 (2000).
[10] O. S. Barišić, Phys. Rev. B **65**, 144301 (2002).
[11] O. S. Barišić, Phys. Rev. B **69**, 064302 (2004).
[12] O. S. Barišić, Phys. Rev. B **73**, 214304 (2006).
[13] G. De Filippis, V. Cataudella, V. Marigliano Ramaglia, and C. A. Perroni, Phys. Rev. B **72**, 014307 (2005).
[14] N. V. Prokof'ev and B. V. Svistunov, Phys. Rev. Lett. **81**, 2514 (1998).
[15] V. Cataudella, G. De Filippis, A. S. Mishchenko, and N. Nagaosa, Phys. Rev. Lett. **99**, 226402 (2007).
[16] B. Lau, M. Berciu, and G. A. Sawatzky, Phys. Rev. B **76**, 174305 (2007).
[17] M. Hohenadler, M. Aichhorn, and W. von der Linden, Phys. Rev. B **68**, 184304 (2003).
[18] M. Berciu and G. L. Goodvin, Phys. Rev. B **76**, 165109 (2007).
[19] G. L. Goodvin, M. Berciu, and G. A. Sawatzky, Phys. Rev. B **74**, 245104 (2006).
[20] J. Bonča, S. A. Trugman, and M. Berciu, Phys. Rev. B **100**, 094307 (2019).
[21] D. Jansen, J. Stolpp, L. Vidmar, and F. Heidrich-Meisner, Phys. Rev. B **99**, 155130 (2019).
[22] W. F. Brinkman and T. M. Rice, Phys. Rev. B **2**, 1324 (1970).
[23] S. A. Trugman, Phys. Rev. B **37**, 1597 (1988).
[24] B. I. Shraiman and E. D. Siggia, Phys. Rev. Lett. **61**, 467 (1988).
[25] L. Vidmar, J. P. Ronzheimer, M. Schreiber, S. Braun, S. S. Hodgman, S. Langer, F. Heidrich-Meisner, I. Bloch, and U. Schneider, Phys. Rev. Lett. **115**, 175301 (2015).
[26] J. P. Ronzheimer, M. Schreiber, S. Braun, S. S. Hodgman, S. Langer, I. P. McCulloch, F. Heidrich-Meisner, I. Bloch, and U. Schneider, Phys. Rev. Lett. **110**, 205301 (2013).
[27] C. Lanczos, J. Res. Natl. Bur. Stand. **45**, 255 (1950).
[28] J. Jaklič and P. Prelovšek, Adv. Phys. **49**, 1 (2000).
[29] P. Prelovšek and J. Bonča, *Ground State and Finite Temperature Lanczos Methods*, Springer Series in Solid-State Sciences, Vol. 176 (Springer-Verlag, Berlin, Heidelberg, 2013), Chap. 1, pp. 1–30.
[30] B. S. Shastry and B. Sutherland, Phys. Rev. Lett. **65**, 243 (1990).
[31] D. Poilblanc, Phys. Rev. B **44**, 9562 (1991).
[32] J. Bonča and P. Prelovšek, Phys. Rev. B **67**, 085103 (2003).
[33] H. Fehske, H. Röder, G. Wellein, and A. Mistriotis, Phys. Rev. B **51**, 16582 (1995).
[34] A. La Magna and R. Pucci, Phys. Rev. B **55**, 14886 (1997).
[35] J. Bonca, T. Katrasnik, and S. A. Trugman, Phys. Rev. Lett. **84**, 3153 (2000).
[36] A. S. Alexandrov, *Polarons in Advanced Materials*, Springer Series in Material Sciences, Vol. 103 (Springer, Dordrecht, 2007).
[37] P. E. Kornilovitch, Europhys. Lett. **59**, 735 (2002).
[38] E. Salje, A. Alexandrov, and W. Liang, *Polarons and Bipolarons in High-T_c Superconductors and Related Materials* (Cambridge University Press, Cambridge, 1995).
[39] A. Alexandrov and N. F. Mott, Rep. Prog. Phys. **57**, 1197 (1994).
[40] A. S. Alexandrov and N. F. Mott, *Polarons and Bipolarons* (World Scientific, Singapore, 1995).